

**Wiley Analytical Science**

# **Wiley Analytical Science Virtual Conference**

**November 9-17**

## **For the 3rd time, The Wiley Analytical Science Conference is back!**

**It's all happening November 9 - 17**

The Wiley Analytical Science Virtual Conference will bring together thousands of researchers and practitioners to share current developments in science and industry. Join for exciting presentations from experts in the fields of analytical and bioanalytical chemistry, pharmaceutical research, materials science, lab automation, and related disciplines.

Register to learn about recent developments & applications in:

- Microscopy
- Spectroscopy
- Mass Spectrometry
- Separation Science
- Much more!

**Register here**

**WILEY**

# Nickel Niobate Anodes for High Rate Lithium-Ion Batteries

Rui Xia, Kangning Zhao, Liang-Yin Kuo, Lei Zhang, Daniel M. Cunha, Yang Wang, Sizhao Huang, Jie Zheng, Bernard Boukamp, Payam Kaghazchi, Congli Sun,\* Johan E. ten Elshof, and Mark Huijben\*

Fast charging is one of the key requirements for next-generation lithium-ion batteries, however, lithium-ion diffusion rates of typical electrode materials are limited. Nanosizing of active electrode material is a common strategy to increase the effective lithium-ion diffusion transport rate, but it also decreases the volumetric energy/power density and stability of the battery. In this work, nickel niobate  $\text{NiNb}_2\text{O}_6$  is demonstrated for the first time as a new intrinsic high-rate anode material for lithium-ion batteries without the requirement of realizing nano-architectures. The  $\text{NiNb}_2\text{O}_6$  host crystal structure exhibits only a single type of channel for lithium-ion intercalation and can be fully lithiated with a capacity of about  $244 \text{ mAh g}^{-1}$  at low current densities. Interestingly, a high diffusion coefficient of  $10^{-12} \text{ cm}^2 \text{ s}^{-1}$  at 300 K enables fast (dis)charging at high current densities resulting in high capacities of 140 and  $50 \text{ mAh g}^{-1}$  for 10 and 100C respectively. The minimal volume change during lithiation is the origin of the stable reversible lithiation process in  $\text{NiNb}_2\text{O}_6$  and leads to 81% capacity retention after 20 000 cycles at 100C. Finally, full cell systems against  $\text{LiFePO}_4$  and  $\text{Li}[\text{Ni}_{0.8}\text{Co}_{0.1}\text{Mn}_{0.1}]\text{O}_2$  (NCM811) cathodes demonstrate the promising energy storage performance of nickel niobate anodes in practical battery devices.

## 1. Introduction

Nowadays, fast charging ability of energy storage devices is essential for applications in electric vehicles and electrical power grids. The fast charging performance of batteries is enabled by high-rate electrode materials, which have been realized through various methods such as nanosizing, porous structures, carbon-coatings, and conductive materials-based hierarchical structures.<sup>[1]</sup> Nanosizing and porous structures can enhance the lithium-ion transport as they reduce the distance lithium ions have to diffuse in the solid electrode, and they also enlarge the contact area between the liquid electrolyte and the electrode material.<sup>[2]</sup> Carbon-coatings and conductive materials (e.g., graphene or Mxene) based hierarchical structures can enhance the electrical conductivity of the electrodes to enable higher current densities.<sup>[3]</sup> However, nanosizing and porous structures

lead to a reduction of the specific volumetric capacity, while composites with carbon-based conductive materials require the electrode to discharge down to 0.01 V resulting in lithium dendrite formation under high current densities.<sup>[4–6]</sup> The formation of nanostructures can even result in a reduced electrochemical performance at high C rates as compared to their bulk materials due to possible morphology change, nanostructure collapse, and higher first-cycle capacity loss.<sup>[7–9]</sup> Furthermore, the fabrication of these delicate nano-architectures, porous structures, and composites usually require harsh synthesis environments, expensive reactants, and multiple synthesis steps, which results in a complex and expensive synthesis process. Additionally, such synthesis methods often provide either relatively low yields or significant amounts of chemical waste.


Recent studies increasingly focus on the development of electrode materials with an intrinsic high-rate performance by combining the advantages of exhibiting 1) a suitable host structure for fast lithium-ion intercalation, 2) a lower bandgap to enhance the electrical conductivity, and 3) a higher working voltage to avoid lithium dendrite formation. Titanium-based oxides, such as  $\text{Li}_4\text{Ti}_5\text{O}_{12}$  and anatase  $\text{TiO}_2$ , are well known as interesting electrode materials, while they exhibit working voltages of 1.55 and 1.8 V,<sup>[10,11]</sup> respectively, preventing lithium plating. However, in order to obtain high rate performance,

R. Xia, D. M. Cunha, Y. Wang, S. Huang, J. Zheng, B. Boukamp, J. E. ten Elshof, M. Huijben  
MESA+ Institute for Nanotechnology  
University of Twente  
P. O. Box 217, Enschede 7500AE, The Netherlands  
E-mail: m.huijben@utwente.nl

K. Zhao, C. Sun  
State Key Laboratory of Advanced Technology for Materials Synthesis and Processing  
International School of Materials Science and Engineering  
Wuhan University of Technology  
Wuhan 430070, China  
E-mail: conglisun@whut.edu.cn

L.-Y. Kuo, P. Kaghazchi  
Forschungszentrum Jülich GmbH  
Institute of Energy and Climate Research  
Materials Synthesis and Processing (IEK-1)  
Jülich 52425, Germany

L. Zhang, C. Sun  
NRC (Nanostructure Research Centre)  
Wuhan University of Technology  
Wuhan 430070, P. R. China

 The ORCID identification number(s) for the author(s) of this article can be found under <https://doi.org/10.1002/aenm.202102972>.

© 2021 The Authors. Advanced Energy Materials published by Wiley-VCH GmbH. This is an open access article under the terms of the Creative Commons Attribution License, which permits use, distribution and reproduction in any medium, provided the original work is properly cited.

DOI: 10.1002/aenm.202102972

nanosizing is still required for these titanium-based oxides. For example, mesoporous yolk-shell anatase  $\text{TiO}_2/\text{TiO}_2(\text{B})$  microspheres reach capacities of  $181 \text{ mAh g}^{-1}$  at a rate of  $40 \text{ C}$ ,<sup>[12]</sup> while hollow multi-shelled heterostructured anatase  $\text{TiO}_2/\text{TiO}_2(\text{B})$  provide capacities of  $125 \text{ mAh g}^{-1}$  at a rate of  $20 \text{ C}$ .<sup>[13]</sup> Furthermore, the band gaps of  $\text{Li}_4\text{Ti}_5\text{O}_{12}$  and anatase  $\text{TiO}_2$  are 3.14 and 3.2 eV, respectively, which still limits the intrinsic electrical conductivity of these electrode materials.

Also, niobium-based oxides, such as T-phase  $\text{Nb}_2\text{O}_5$  and niobium tungsten oxides, have attracted attention because of their high rate performance. Porous T- $\text{Nb}_2\text{O}_5$  nanoflowers can provide  $130 \text{ mAh g}^{-1}$  specific capacity at  $5 \text{ A g}^{-1}$  due to its high ionic diffusivity,<sup>[14]</sup> while the specific capacity of T- $\text{Nb}_2\text{O}_5$  nanocrystals can reach  $40 \text{ mAh g}^{-1}$  at  $1000 \text{ C}$ <sup>[15]</sup> as enabled by its lithium-ion intercalation pseudo-capacitance. More recently, niobium tungsten oxides have shown high rate capabilities caused by its suitable host structure for lithium-ion diffusion. For example,  $\text{Nb}_{14}\text{W}_3\text{O}_{44}$ <sup>[16]</sup> and  $\text{Nb}_{18}\text{W}_{16}\text{O}_{93}$ <sup>[17]</sup> bulk particles reach 57 and  $70 \text{ mAh g}^{-1}$  at  $100 \text{ C}$ , respectively. Unfortunately, the niobium tungsten oxide structure contains multiple types of channels, which results in multiple voltage plateaus and is, therefore, inconvenient for practical usage. Furthermore, the achieved specific capacity at high C rates is still relatively low when taking into account the required capacities for practical high-rate storage devices. Interestingly, nanosizing of these niobium tungsten oxides into nanowires enhances its rate performance and cycling stability, as  $\text{Nb}_{14}\text{W}_3\text{O}_{44}$ ,<sup>[18]</sup>  $\text{Nb}_{18}\text{W}_{16}\text{O}_{93}$ ,<sup>[19]</sup> and  $\text{Nb}_8\text{W}_9\text{O}_{47}$ <sup>[20]</sup> nanowires exhibited specific capacities of 130 (6.7 C), 153 (6.7 C), and  $113 \text{ mAh g}^{-1}$  (5 C), respectively. However, ideal high-rate electrode materials should intrinsically exhibit fast lithium-ion diffusion with a single voltage plateau without complex synthesis procedures to minimize the length scales for lithium diffusion in nano-architectures.

In this work, we demonstrate nickel niobate,  $\text{NiNb}_2\text{O}_6$ , as a new electrode material, which exhibits an intrinsic high rate performance enabled by its suitable host crystal structure, as shown in **Figure 1**, and its large pseudo-capacitance. The  $\text{NiNb}_2\text{O}_6$  columbite structure contains a single type of channel for lithium-ion intercalation, which leads to a single voltage plateau at 1.6–1.7 V during charge-discharge cycling, facilitating

use in practical high-rate lithium-ion batteries. The oxidation of all three transition metal ions enables the structure to fully lithiate up to  $\text{Li}_3\text{NiNb}_2\text{O}_6$  with a capacity of about  $244 \text{ mAh g}^{-1}$  at 0.5C. Faster (dis)charging at 1, 5, 10, and  $100 \text{ C}$  resulted in high capacities of respectively 220, 165, 140, and  $50 \text{ mAh g}^{-1}$ . The stability of the reversible lithiation process in  $\text{NiNb}_2\text{O}_6$  is demonstrated by achieving a capacity retention of 81% after 20 000 cycles at 100C. The structural stability and electrochemical behavior, with a high diffusion coefficient of  $10^{-12} \text{ cm}^2 \text{ s}^{-1}$ , were investigated by various experimental techniques and confirmed by density functional theory (DFT) calculations. Finally, full cell systems against  $\text{LiFePO}_4$  and NCM811 cathodes demonstrated the promising energy storage performance of  $\text{NiNb}_2\text{O}_6$  anodes in practical battery devices.

## 2. Results and Discussion

### 2.1. Structural Characterization

Nickel niobate,  $\text{NiNb}_2\text{O}_6$ , typically forms a columbite phase (Pbcn)<sup>[21,22]</sup> exhibiting an orthorhombic crystal structure with lattice parameters of 14.022, 5.675, and  $5.015 \text{ \AA}$  (JCPDS card: No. 01-072-0481), as schematically depicted in **Figure 1**. In this orthorhombic structure the oxygen atoms form corner-shared octahedra around the  $\text{Ni}^{2+}$  and  $\text{Nb}^{5+}$  ions, creating isolated zig-zag chains of Ni ions. As there are four formula units per crystallographic unit cell, the structure consists of layers of  $\text{NiO}$  octahedra at  $x = 0$  and  $x = 0.5$  which are separated by two intervening  $\text{NbO}_6$  layers. However, previous studies have also demonstrated the formation of disordered rutile ( $\text{P4}_2/\text{mnm}$ )<sup>[23]</sup> and tetragonal ( $\text{P4}_2/\text{n}$ )<sup>[24]</sup> polymorphs. X-ray diffraction (XRD) analysis of our synthesized particles confirmed the formation of the orthorhombic  $\text{NiNb}_2\text{O}_6$  structure, as shown in **Figure 2a**.

The morphology and size of the synthesized  $\text{NiNb}_2\text{O}_6$  particles were investigated by scanning electron microscopy (SEM). The agglomerated particle size is in the range 1–5  $\mu\text{m}$  (**Figure S1a**, Supporting Information), while the single primary particle size is mainly between 0.3 and 0.8  $\mu\text{m}$  (**Figure 1b**). The agglomerated particles are formed by stacking of the irregular polyhedron-shaped

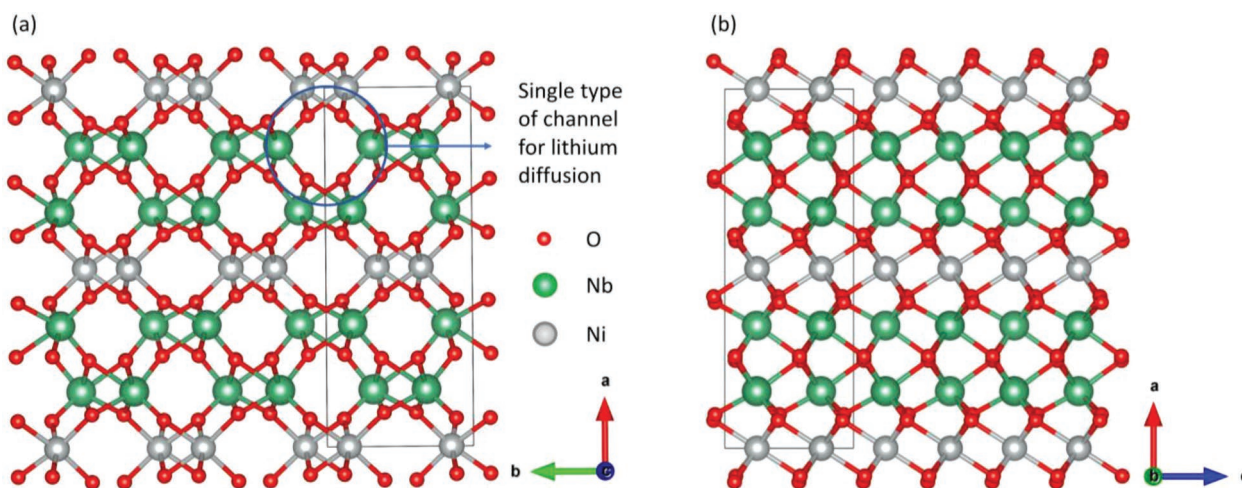


**Figure 1.** a,b) Schematic diagrams of the  $\text{NiNb}_2\text{O}_6$  host structure.

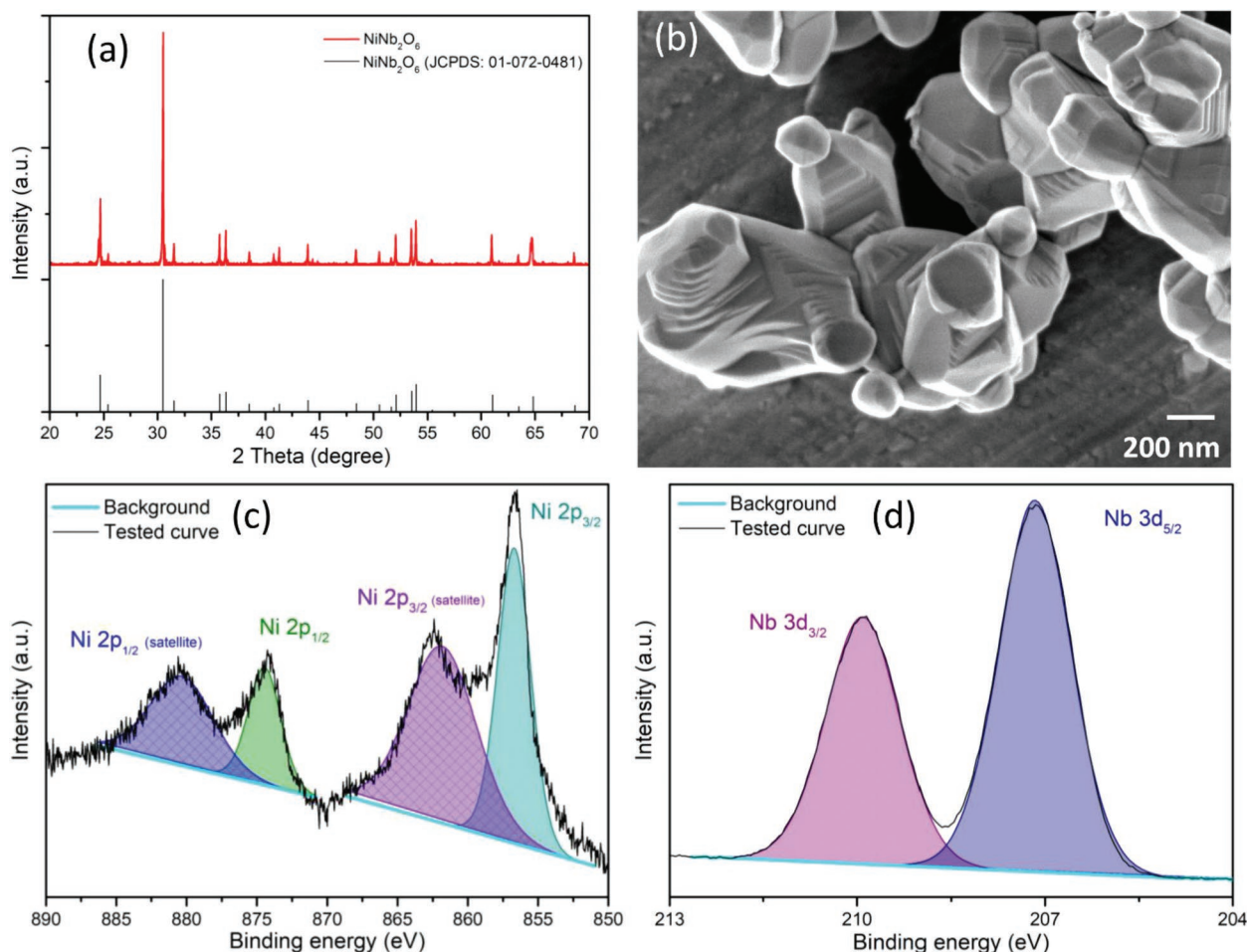


**Figure 2.** Structural characterization of the pristine  $\text{NiNb}_2\text{O}_6$  powder by a) X-ray Diffraction, b) SEM analysis, and c,d) XPS spectra of 2p nickel and 3d niobium levels, respectively.

primary particles. The layered structure of the  $\text{NiNb}_2\text{O}_6$  phase can be observed in Figure S1b, Supporting Information, which confirms the successful formation of the orthorhombic structure exhibiting a layered structure along the  $a$ -axis. Furthermore, the average size of the particles was determined by Brunauer–Emmett–Teller method (BET) analysis in which nitrogen adsorption at different pressures enables determination of the specific surface area of the  $\text{NiNb}_2\text{O}_6$  powder ( $1.554 \pm 0.003 \text{ m}^2 \text{ g}^{-1}$ ), see Figure S2, Supporting Information. Using a spherical model to express the  $\text{NiNb}_2\text{O}_6$  powder, the average diameter of the particles was calculated to be  $680 \pm 1 \text{ nm}$  (Table S1, Supporting Information), which matches very well with the observations by SEM analysis. The composition of the  $\text{NiNb}_2\text{O}_6$  powder was investigated by X-ray fluorescence spectroscopy (XRF) analysis, which confirmed the exact 1:2 atomic ratio between Ni and Nb (Table S2, Supporting Information), which agrees well with the  $\text{NiNb}_2\text{O}_6$  phase measured by XRD (Figure 2a). X-ray photoelectron spectroscopy (XPS) analysis of the as-prepared  $\text{NiNb}_2\text{O}_6$  powder shows the Ni  $2p_{3/2}$  peak at 856.7 eV and the Nb  $3d_{5/2}$  peak at 207.1 eV (Figure 2c,d), which confirms the expected  $\text{Ni}^{2+}$  and  $\text{Nb}^{5+}$  oxidation states.<sup>[25,26]</sup> Furthermore, XPS analysis was performed on cycled  $\text{NiNb}_2\text{O}_6$  electrodes at 1.7 and 1.0 V discharged states, as shown in Figure S3, Supporting Information. In comparison to the valence

state of niobium in pristine  $\text{NiNb}_2\text{O}_6$  (Figure 2d),  $\text{Nb}^{5+}$  is gradually reduced to  $\text{Nb}^{4+}$  during the discharge process down to 1.0 V (Figure S3c, Supporting Information), while both  $\text{Nb}^{5+}$  and  $\text{Nb}^{4+}$  are present halfway the discharge process at 1.7 V (Figure S3a, Supporting Information). At the same time the  $\text{Ni}^{2+}$  peak shifts to a lower binding energy, while  $\text{Ni}^0$  is also present in the  $\text{NiNb}_2\text{O}_6$  samples discharged to 1.7 and 1.0 V (Figure S3b,S3d, Supporting Information). Although the multiple peak profile of  $\text{Ni}^{2+}$  warrants further investigation, we may conclude that both Ni and Nb contribute to the redox reactions for lithium storage.

To determine the variations in the  $\text{NiNb}_2\text{O}_6$  unit cell lattice during lithiation, operando XRD analysis was performed while cycling a mixed  $\text{NiNb}_2\text{O}_6$  electrode in a half cell against lithium metal at C/8 within the 1.0 to 3.0 V range (Figure 3a). It can be observed that the  $\text{NiNb}_2\text{O}_6$  (311) diffraction peak shifts following the charge-discharge process (Figure 3b). By using Gaussian fitting the peak position was determined (Figure 3c), which indicates a reversible shift by 0.03 degrees between the charged and discharged states. These results suggest that the lithium intercalation only causes 0.112% widening between the (311) Miller planes. This minimal change suggests that the crystal structure of nickel niobate is quite stable during the charge-discharge process, which is ideal for fast lithium diffusion.

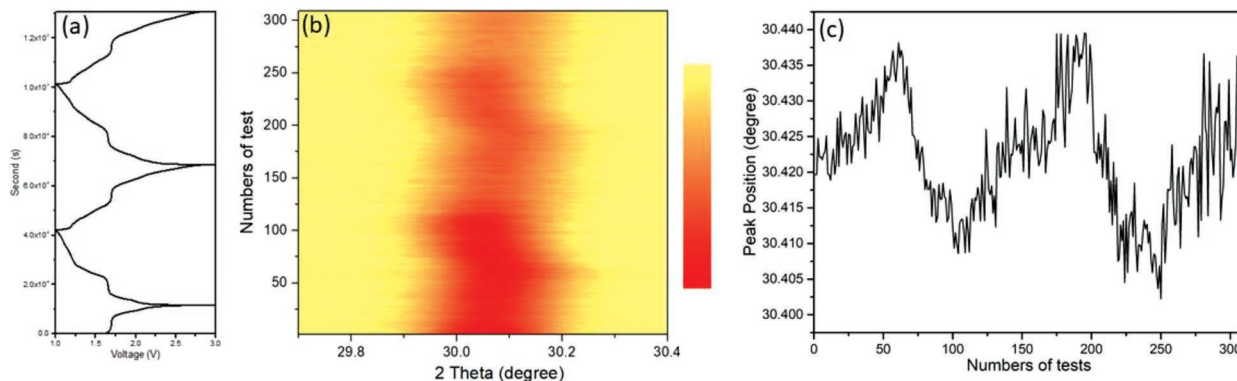


**Figure 3.** Single peak operando XRD analysis of  $\text{NiNb}_2\text{O}_6$  electrode in a half cell against lithium metal. a) Voltage versus time profile of two consecutive charge-discharge cycles at  $C/8$  within 1.0 to 3.0 V range. b) Repetitive  $\Omega$ - $2\theta$  scans of (311) peak during electrochemical cycling. c) (311) peak position changes during charge-discharge process.

The observed structural changes in the  $\text{NiNb}_2\text{O}_6$  crystal structure during lithium intercalation were studied in detail by ex situ scanning transmission electron microscopy (STEM) analysis after cycling of the mixed electrode material in a half cell against lithium metal (Figure 4). Specimens were obtained through focused ion beam along different crystal directions for electrode materials at different voltage states (3, 1.7, and 1 V, representing  $\text{NiNb}_2\text{O}_6$ ,  $\text{Li}_{1.5}\text{NiNb}_2\text{O}_6$ , and

$\text{Li}_3\text{NiNb}_2\text{O}_6$  respectively) from the  $\text{NiNb}_2\text{O}_6$  host structure until the fully lithiated  $\text{Li}_3\text{NiNb}_2\text{O}_6$  structure. The STEM images in Figure 4a–c show projections along the (013) Miller plane for the 3 V specimen, along the (311) plane for the 1.7 V specimen, and along the (100) plane for the 1 V specimen. The corresponding strain mappings in Figure 4d–f indicate that the strain inside the crystal lattice is always located in between the layers containing the transition metal ions (Ni and Nb).

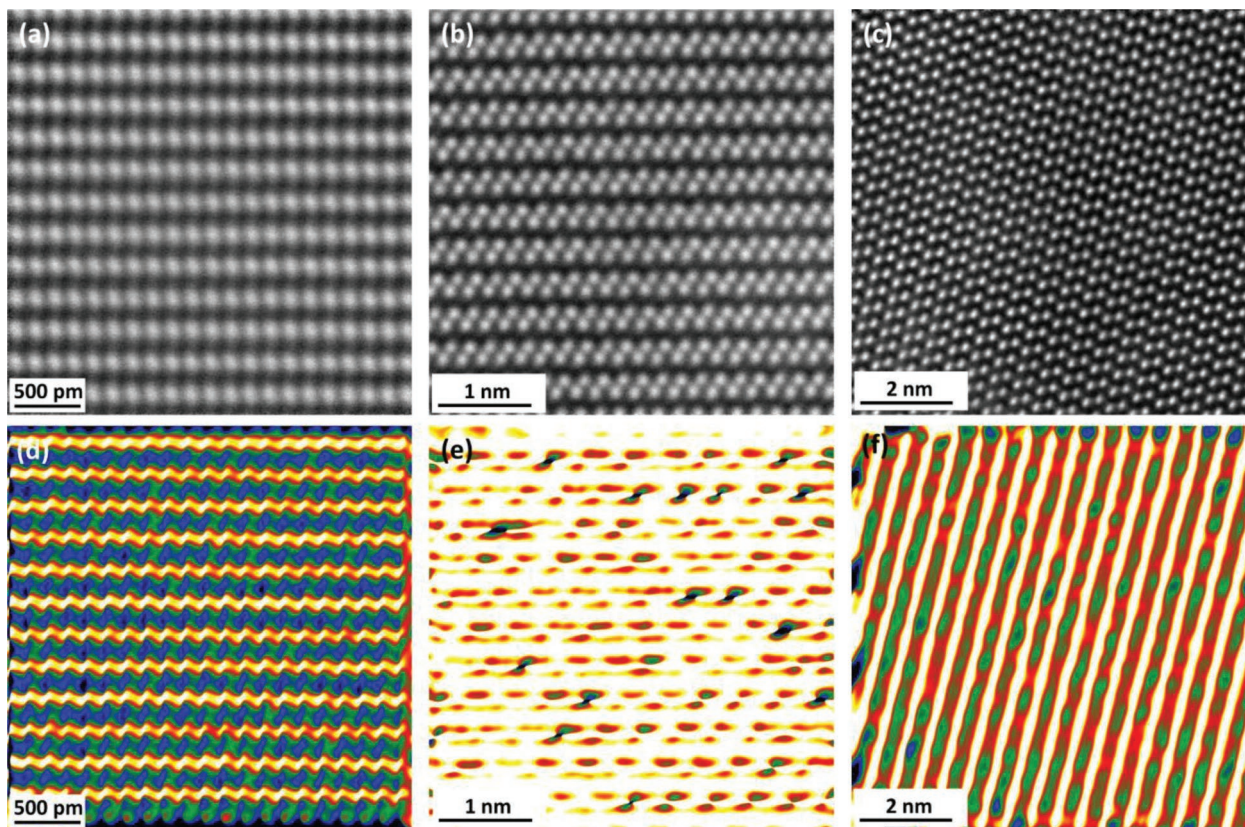


**Figure 4.** Ex situ STEM analysis of a  $\text{NiNb}_2\text{O}_6$  powder after cycling in a half cell against lithium metal. a–c) Images of specimens at different voltage states (3, 1.7, and 1 V, respectively) from the  $\text{NiNb}_2\text{O}_6$  host structure until the fully lithiated structure with projections along the (013), (311), and (100) Miller planes, respectively. d–f) Strain mappings of the specimens at different voltage states (3, 1.7, and 1 V, respectively).

This means that the lattice strain is strictly trapped in between the transition metal ion layers and doesn't develop upon lithium-ion intercalation, resulting in a very stable crystal structure with minimal volume expansion, in good agreement with experimental XRD results. Furthermore, Figure S4a–c, Supporting Information, shows that grain boundaries can be found in the pristine and cycled NiNb<sub>2</sub>O<sub>6</sub> powders, which may contribute to the lithium-ion diffusion in NiNb<sub>2</sub>O<sub>6</sub> electrodes.

## 2.2. Theoretical Modeling

To find the most favorable site for a single Li-ion in NiNb<sub>2</sub>O<sub>6</sub> (modeled by a 1 × 1 × 2 unit cell: Li<sub>1</sub>Ni<sub>8</sub>Nb<sub>16</sub>O<sub>48</sub>), we considered all possible configurations with 1 Li<sup>+</sup> in 34 possible interstitial sites (with a minimum distance of 1.6–2.0 Å with respect to nearest neighbors) as well as 1 Ni<sup>1+</sup> and 7 Ni<sup>2+</sup> in 8 Ni sites, namely,  $\frac{34!}{1!33!} \cdot \frac{8!}{7!1!} = 272$  structures. Total Coulomb energies  $E_c$  of 272 structures were calculated using elementary charges of 1+ for Li, 5+ for Nb, and 2- for O. By performing density function theory perdue–burke–ernzerhof (DFT-PBE) calculations on 10 distinguishable topmost electrostatically favorable structures it was found that the lowest total energy structure is the one with the lowest  $E_c$ , and that Li prefers occupying octahedral sites. Our ab initio molecular dynamics (AIMD) simulation showed that the most favorable pathway for Li-ion migration is along the *c* direction. Subsequently, DFT nudged elastic band (DFT-NEB) calculations were used to compute the diffusion barrier  $E_b$  along the *c* direction (Figure S5, Supporting Information) to be 0.46 eV. Our computed  $E_b$  value is similar to the previously calculated (using DFT or MD) energy barrier of the rate-limiting step for the diffusion of Li in the anatase phase of TiO<sub>2</sub> ( $E_b = 0.496$  eV),<sup>[27]</sup> TT-Nb<sub>2</sub>O<sub>5</sub> ( $E_b = 0.46$  eV),<sup>[28]</sup> and T-Nb<sub>2</sub>O<sub>5</sub> ( $E_b = 0.47$  eV)<sup>[28]</sup> considering a low Li concentration.

Using the transition state theory, the diffusion coefficient was then computed by

$$D = \frac{w}{2d} \nu l^2 \exp\left(-\frac{E_b}{k_B T}\right) \quad (1)$$

where  $w$  and  $d$  are the number of nearest neighbor sites for Li hopping and dimensionality of diffusion, which are 2 and 1, respectively, for NiNb<sub>2</sub>O<sub>6</sub>.  $\nu$  is the frequency of a successful jump between successive Li sites (i.e., jump frequency) and was calculated using the harmonic transition state theory approximation

$$\nu = \frac{\prod_1^{3N} \nu_i^G}{\prod_1^{3N-1} \nu_i^T} \quad (2)$$

Here,  $\nu_i^G$  and  $\nu_i^T$  are the real vibrational frequencies (computed by DFT-PBE calculations) of the ground and transition state, respectively. With a distance of 2.14 Å between two adjacent Li sites ( $l$ ) and  $\nu = 1.36 \times 10^{13}$  Hz the diffusion coefficient  $D$  was calculated to be  $1.16 \times 10^{-10}$  cm<sup>2</sup> s<sup>-1</sup> for bulk Li<sub>0.125</sub>NiNb<sub>2</sub>O<sub>6</sub> at room temperature (300 K). Our computed diffusion coefficient for this system is higher than the previously calculated value of  $5.25 \times 10^{-12}$  cm<sup>2</sup> s<sup>-1</sup> for diffusion of Li in TiO<sub>2</sub>-anatase with a low Li concentration at 300 K.<sup>[27]</sup>

## 2.3. Electrochemical Characterization

Electrochemical measurements were performed to determine the performance of NiNb<sub>2</sub>O<sub>6</sub> as electrode material for fast charging, high-capacity lithium-ion batteries. Galvanostatic charge-discharge cycling was used to investigate the cycle life of NiNb<sub>2</sub>O<sub>6</sub> mixed electrodes (8:1:1 mass ratio). The average voltage of the charge and discharge plateaus is about 1.6 V when cycling at a rate of 1 C, which increases gradually for higher rates of 5C and 10C to respectively 1.65 and 1.72 V (Figure S6, Supporting Information). The initial capacities of these NiNb<sub>2</sub>O<sub>6</sub> mixed electrodes at 1, 10, and 100 C are 231, 126, and 60 mAh g<sup>-1</sup>, respectively, as shown in Figure 5a–c. Interestingly, the specific capacity of NiNb<sub>2</sub>O<sub>6</sub> at 1 C is 97.8% of its theoretical capacity, which indicates that the NiNb<sub>2</sub>O<sub>6</sub> host structure can be almost fully lithiated up to Li<sub>3</sub>NiNb<sub>2</sub>O<sub>6</sub>. This suggests the oxidation of all three transition metal ions in the NiNb<sub>2</sub>O<sub>6</sub> structure within the used voltage range between 1.0 and 3.0 V.

The cycle life performance was investigated for different rates of 1, 10, and 100 C (23.6 A g<sup>-1</sup>) for 300, 2500, and 20000 cycles, respectively (Figure 5a–c), showing good capacity retentions of 97%, 92%, and 81%, respectively. Furthermore, the Coulombic efficiencies in all measurements were stable with values between 99.8 and 100.2%. This high cycling stability demonstrates the stable, reversible lithiation process in NiNb<sub>2</sub>O<sub>6</sub> up to very high current densities, and confirms that NiNb<sub>2</sub>O<sub>6</sub> is a promising candidate material for high rate electrodes in lithium-ion batteries.

More detailed rate performance measurements were performed on a mixed NiNb<sub>2</sub>O<sub>6</sub> electrode (7.5:1.5:1 mass ratio) in a half cell against lithium metal for various current densities between 0.5 and 100 C (Figure 5d). The overall rate performance results show that the NiNb<sub>2</sub>O<sub>6</sub> electrode can cycle very stable from a low current density (244 mAh g<sup>-1</sup> for 0.5 C) up to a high current density (100 C), and subsequently back to 1 C resulting in a specific capacity (219.8 mAh g<sup>-1</sup> after 150 cycles) which is very similar to the initial specific capacity at 1 C (219.2 mAh g<sup>-1</sup> after the first 20 cycles). In comparison to the capacity at 0.5C the capacity retentions at higher C rates (1, 2, 5, 10, 20, 50, and 100 C), are respectively 220, 200, 165, 140, 117, 82, and 50 mAh g<sup>-1</sup> (e.g., 90.1%, 81.6%, 67.6%, 57.4%, 47.8%, 33.6%, and 20.1%, respectively). Furthermore, the charge-discharge curves show clear voltage plateaus, which are increasing in voltage for higher current densities (Figure 5e). This indicates that the observed capacity decrease for higher current densities originates from an increasing polarization (concentration polarization and electrochemical polarization) creating an enhanced overpotential. It confirms that the NiNb<sub>2</sub>O<sub>6</sub> crystal structure remains stable even after charge-discharge cycling at very high current densities, in good agreement with results from our XRD and STEM analysis.

In order to investigate the influence of the electrode resistance to the rate performance of NiNb<sub>2</sub>O<sub>6</sub> electrode material, a mixed NiNb<sub>2</sub>O<sub>6</sub> electrode (8:1:1 mass ratio) with a slightly lower carbon black contribution was studied as well (Figure S7, Supporting Information). It showed a similar rate performance as compared to the 7.5:1.5:1 mass ratio NiNb<sub>2</sub>O<sub>6</sub> electrode (Figure 5) for rates below 20 C. However, for rates of 50 and 100 C, the 7.5:1.5:1 mass ratio NiNb<sub>2</sub>O<sub>6</sub> electrode provided a

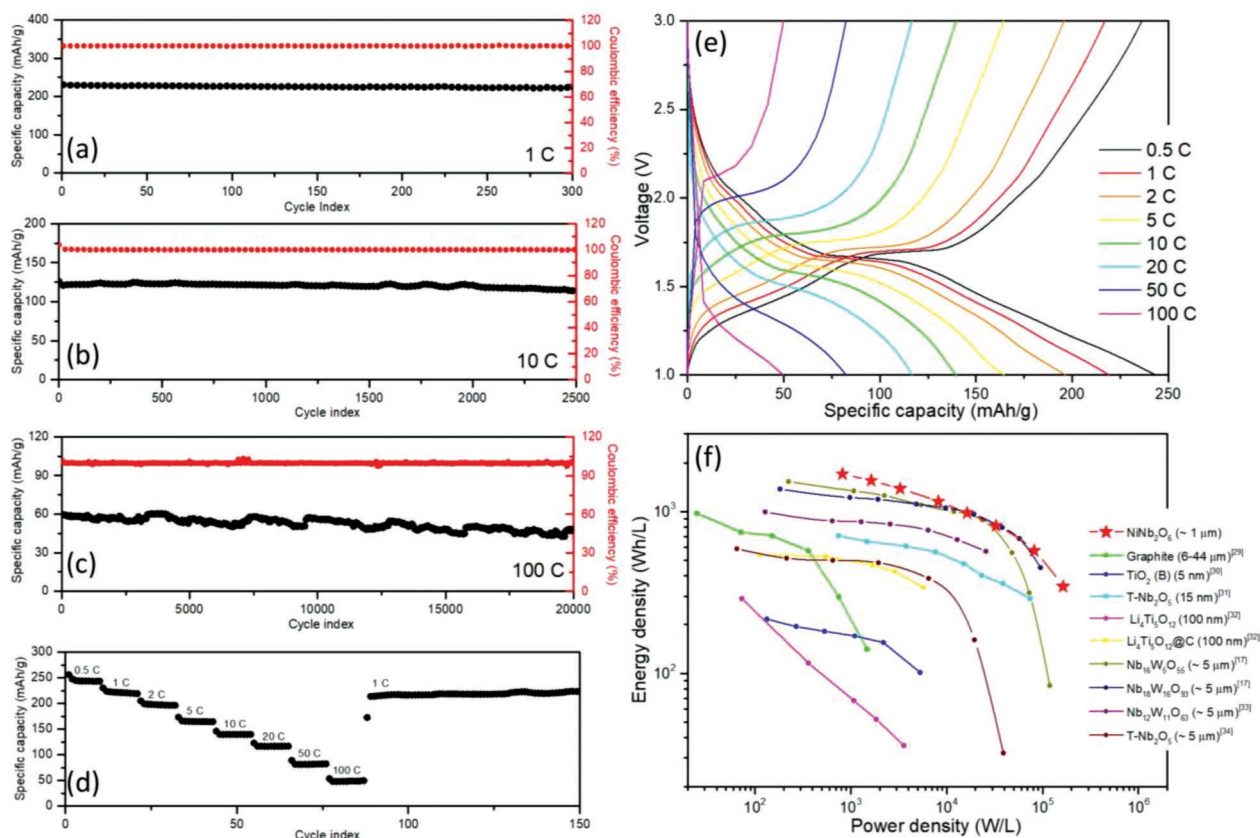


**Figure 5.** Electrochemical performance of a mixed  $\text{NiNb}_2\text{O}_6$  electrode in a half cell against lithium metal. a–c) Galvanostatic charge-discharge cycling at respectively 1, 10, and 100 C. d) Specific discharge capacity versus cycle number profile for different rates between 0.5 and 100 C. e) Voltage versus specific capacity charge-discharge profiles at different rates. f) Volumetric Ragone plot comparing our results to previous studies.<sup>[17,29–34]</sup>

higher capacity retention than the 8:1:1 mass ratio electrode. This means that a decrease of the resistance by adding 5% more conductive carbon will only show a significant effect for ultrafast charging above 20 C.

The advantage of an intrinsic high-rate electrode material, as compared to nano-sized electrode materials, is most pronounced in the volumetric energy and power densities. Nano-sizing of electrode materials requires an increase in the amount of conductive carbon to provide an optimal conductive network, which has a minimal effect on the weight (i.e., gravimetric densities) but a large effect on the volume, and therefore, the volumetric densities. To compare our results for  $\text{NiNb}_2\text{O}_6$  electrodes with previously reported high-rate anode materials a volumetric Ragone plot is shown in Figure 5f. It can be seen that  $\text{NiNb}_2\text{O}_6$  exhibits higher energy densities for the full power density range outperforming all other reported materials, and only in the middle power density region, the energy density of  $\text{NiNb}_2\text{O}_6$  is similar to  $\text{Nb}_{18}\text{W}_{16}\text{O}_{93}$ .<sup>[17]</sup>

To obtain more in-depth knowledge on lithium-ion intercalation in  $\text{NiNb}_2\text{O}_6$  the electrochemical diffusion coefficient of lithium ions in the  $\text{NiNb}_2\text{O}_6$  structure was experimentally determined by three different methods: different sweep rate Cyclic Voltammetry (CV), Galvanostatic Intermittent Titration Technique (GITT), and Electrochemical Impedance Spectroscopy (EIS). For the CV measurements four different sweep rates (0.1, 0.2, 0.5, and 1  $\text{mV s}^{-1}$ ) were used leading to a dominant

reaction peak around 1.7 V during charge and discharge (Figure 6a), in good agreement with the voltage plateaus in Figure 5e. At around 1.1 V, a small peak can be observed which suggests that after  $\text{Nb}^{5+}$  to  $\text{Nb}^{4+}$  reduction, a small amount of  $\text{Nb}^{4+}$  is further reduced to  $\text{Nb}^{3+}$ , although this was not observed during XPS analysis for the sample at the 1 V discharged state. The linear fit of the peak currents during lithiation and delithiation versus the square root sweep rate is shown in Figure 6b from which lithium-ion diffusion coefficients of  $1.20 \times 10^{-12}$  (lithiation) and  $1.36 \times 10^{-12} \text{ cm}^2 \text{ s}^{-1}$  (delithiation) can be calculated<sup>[35]</sup> (Figure S8, Supporting Information). Furthermore, following Dunn's model<sup>[36]</sup> the  $b$ -value above 0.75 can be determined outside the peak voltage region close to 1.7 V (Figure 6c). This  $b$ -value is an indication of the storage mechanism, and suggests that this  $\text{NiNb}_2\text{O}_6$ -based battery is a hybrid device and its capacity originates from intercalation and as well as from pseudo-capacitance.

The pseudocapacitive contribution to the storage capacity was investigated in more detail to determine its importance for the lithium storage ability of  $\text{NiNb}_2\text{O}_6$  electrodes. The calculation result for 0.5  $\text{mV s}^{-1}$  sweep rate using Dunn's model<sup>[36]</sup> shows a high pseudocapacitive contribution (Figure 6d), which explains the excellent rate performance. The pseudocapacitive contribution ratio is increasing with increasing sweep rates up to 82.3% at 1  $\text{mV s}^{-1}$  (Figure 6e), which is similar to nanosized niobates.<sup>[37]</sup> However, the  $\text{NiNb}_2\text{O}_6$  material under investigation

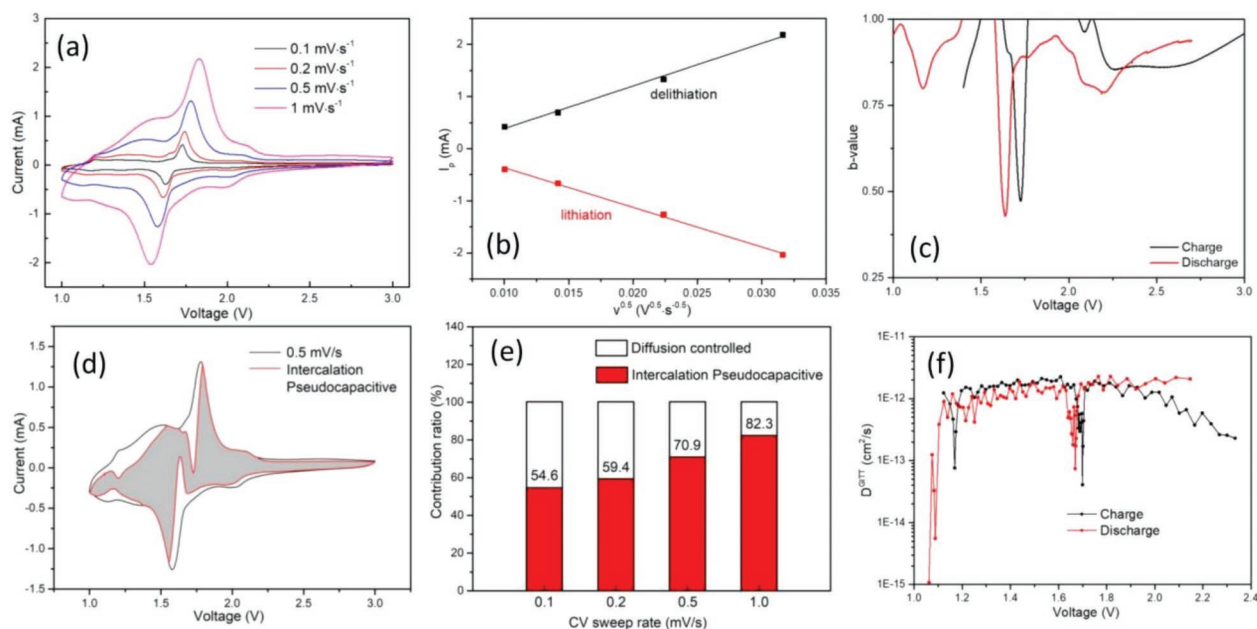


**Figure 6.** Lithium-ion diffusion analysis for a mixed  $\text{NiNb}_2\text{O}_6$  electrode in a half cell against lithium metal. a) CV analysis at different sweep rates ( $0.1\text{--}1.0\text{ mV s}^{-1}$ ). b) Peak current versus square root sweep rate fits during lithiation and delithiation. c)  $b$ -value versus voltage profiles from different sweep rate CV measurements. d) Lithium-ion intercalation pseudocapacitive contribution from CV curve at  $0.5\text{ mV s}^{-1}$ . e) Lithium-ion intercalation pseudocapacitive contribution ratio in different sweep rate CV measurements. f) GITT analysis of lithium-ion diffusion coefficients during charging and discharging process.

here still remains a bulk powder with particle sizes of about 680 nm (Table S1, Supporting Information). This shows that the host structure of  $\text{NiNb}_2\text{O}_6$  crystal is suitable for lithium-ion intercalation, which indicates that this intercalation charge storage process is not limited by lithium-ion diffusion but by the surface process. Thus, the overall capacitive behavior of  $\text{NiNb}_2\text{O}_6$  can be explained by its lithium-ion intercalation pseudocapacitive property. The results of the GITT measurements yield calculated<sup>[38]</sup> (Figure S9, Supporting Information) lithium-ion diffusion coefficients of about  $1\text{--}2 \times 10^{-12}\text{ cm}^2\text{ s}^{-1}$  (Figure 6f) during the charge-discharge process, in good agreement with the values calculated from the different sweep rate CV.

EIS measurements were also performed for mixed  $\text{NiNb}_2\text{O}_6$  electrodes in the charged and discharged state, and fitted to equivalent circuit models to determine the different contributions. For the discharged state (Figure 7a) the circuit contains a bulk resistance ( $R_b$ ), a separator component, and a charge transfer component.<sup>[39]</sup> The fit suggests that the resistance of the  $\text{Li}_3\text{NiNb}_2\text{O}_6$  electrode is about  $9.9 \pm 0.24\ \Omega\text{ cm}^{-2}$ . For the charged state (Figure 7b) the EIS measurement is fitted with a different circuit containing a bulk resistance, a separator component, and two charge transfer components, which suggests the existence of a solid-liquid charge transfer at the solid-electrolyte interface as well as a solid-solid charge transfer in

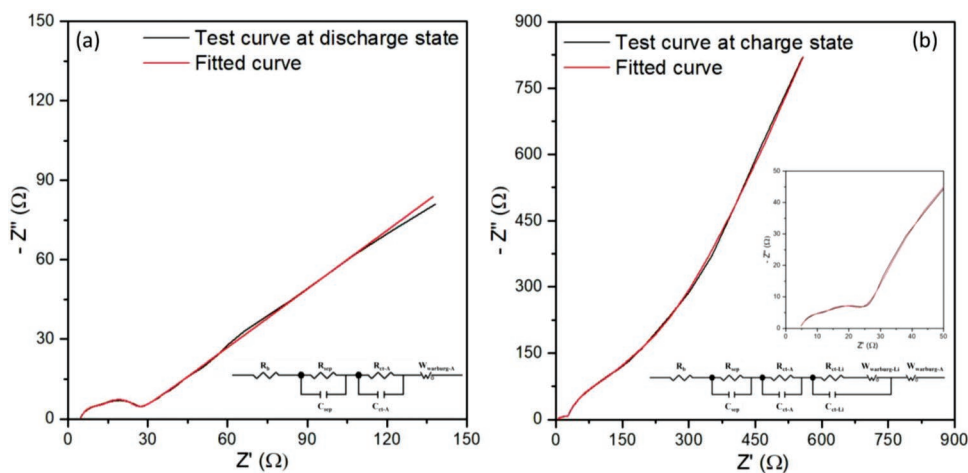


**Figure 7.** Lithium-ion diffusion analysis for a mixed  $\text{NiNb}_2\text{O}_6$  electrode in a half cell against lithium metal. EIS analysis in a) the discharged stage and in b) the charged state. The fitting curves are also shown, as well as the equivalent circuit models applied for the fits. The inset shows a zoom-in for the charged state.



between the  $\text{NiNb}_2\text{O}_6$  bulk particles. The results suggest that the resistance of the  $\text{NiNb}_2\text{O}_6$  electrode is  $76 \pm 0.34 \Omega$ . This means that the variation in resistance between the charged  $\text{NiNb}_2\text{O}_6$  phase and the discharged  $\text{Li}_3\text{NiNb}_2\text{O}_6$  phase is very minimal, which is ideal for fast charging electrode materials.

The lithium-ion diffusion coefficients were calculated from the Warburg part of the EIS spectra, as described in detail in the supporting information. We used the method proposed by Ho et al.<sup>[40]</sup> in which the slopes of  $Z'$  versus  $\omega^{-0.5}$  curves are obtained by linear fits (Figure S10, Supporting Information) and the slopes of the potential versus the numbers of lithium-ions inside the  $\text{NiNb}_2\text{O}_6$  structure are obtained by the deviation of the potential versus numbers of lithium-ion curves (Figure S11, Supporting Information). The lithium-ion diffusion coefficients calculated from the EIS spectra are  $3.96 \times 10^{-12} \text{ cm}^2 \text{ s}^{-1}$  for the discharged state and  $1.21 \times 10^{-12} \text{ cm}^2 \text{ s}^{-1}$  for the charged state. This confirms that the electrochemical lithium-ion diffusion coefficient of the  $\text{NiNb}_2\text{O}_6$  electrode is in the  $10^{-12} \text{ cm}^2 \text{ s}^{-1}$  range, in close agreement with the CV and GITT results. To demonstrate the unique high lithium-ion diffusion coefficient in our  $\text{NiNb}_2\text{O}_6$  material, a comparison with other high rate anode materials is shown in Table S3, Supporting Information. Fast charging bulk materials, such as titanium- and niobium-based oxides, typically exhibit one or two orders of magnitude lower lithium-ion diffusion coefficients ( $10^{-13}$ – $10^{-14} \text{ cm}^2 \text{ s}^{-1}$ ),<sup>[18–20,35,41–44]</sup> while only nanosizing  $\text{Nb}_8\text{W}_9\text{O}_{47}$  down to 50 nm wide nanowires has yielded similar values of about  $10^{-12} \text{ cm}^2 \text{ s}^{-1}$ .<sup>[20]</sup>

## 2.4. Practical Battery Performance

In order to investigate the electrochemical behavior of  $\text{NiNb}_2\text{O}_6$  electrodes under practical conditions, several experiments were performed on thick  $\text{NiNb}_2\text{O}_6$  electrodes with practical loading (about  $8.5 \text{ mg cm}^{-2}$ ,  $2 \text{ mAh cm}^{-2}$ ) including half-cell measurements, full cell measurements against commercial cathode materials, and finally experiments with a lean electrolyte contribution. The rate performance of a high loading ( $\approx 8.5 \text{ mg cm}^{-2}$ )  $\text{NiNb}_2\text{O}_6$  electrode in a half cell against lithium metal shows similar capacity retention behavior (specific capacity at 20 C is around 50% of the capacity at 1C, Figure S12a, Supporting Information) as compared to the commonly used low loading ( $1\text{--}3 \text{ mg cm}^{-2}$ ) for electrochemical performance analysis of high rate electrode materials in other scientific studies. Although the capacity retention for high loading  $\text{NiNb}_2\text{O}_6$  electrodes is reduced for high rates above 20 C (Figure S12a, Supporting Information) as compared to low loading  $\text{NiNb}_2\text{O}_6$  electrodes (Figure 5d) due to increased internal resistance, they can still deliver  $90 \text{ mAh g}^{-1}$  ( $0.77 \text{ mAh cm}^{-2}$ ) in a charge-discharge process of only 70 s. The charge-discharge profiles of such high loading  $\text{NiNb}_2\text{O}_6$  electrode (Figure S12b, Supporting Information) for different rates show that the voltage bias between the charge and discharge plateaus is larger than the for the low loading  $\text{NiNb}_2\text{O}_6$  electrode (Figure 5e), which confirms the higher internal resistance in these large loading  $\text{NiNb}_2\text{O}_6$  electrodes. The cycle life of the high loading  $\text{NiNb}_2\text{O}_6$  electrode was also investigated and no capacity loss was observed after 100 cycles at a 1 C rate (Figure S12c, Supporting Information),

which suggests that  $\text{NiNb}_2\text{O}_6$  is a promising electrode material for practical applications for which high loading is required.

However, for  $\text{NiNb}_2\text{O}_6$  to be applied as a fast-charging anode material in a real battery device, it needs to be combined with a standard cathode material commonly used in commercial lithium-ion batteries, such as  $\text{LiFePO}_4$  (LFP) and  $\text{LiNi}_{0.8}\text{Co}_{0.1}\text{Mn}_{0.1}\text{O}_2$  (NCM811). The redox reactions during (de)lithiation in LFP, NCM811, and  $\text{NiNb}_2\text{O}_6$  typically occur at 3.5, 3.9, and 1.7 V, respectively, resulting in the voltage plateaus when cycled against lithium metal (Figure S13a, Supporting Information). Therefore, the electrochemical behavior of the two different full cells was analyzed in different voltage ranges: the LFP| $\text{NiNb}_2\text{O}_6$  cell between 1.0 and 2.5 V and the NCM811| $\text{NiNb}_2\text{O}_6$  cell between 1.0 and 2.8 V. The voltage plateau of the LFP| $\text{NiNb}_2\text{O}_6$  cell is indeed at the expected 1.8 V (Figure 8a). Cycle life analysis of the LFP| $\text{NiNb}_2\text{O}_6$  cell at 5 C shows after 200 cycles a high specific capacity of  $140.2 \text{ mAh g}^{-1}$  and outstanding cycling stability with a capacity retention of 96.3% and a constant coulombic efficiency of about 99.8% (Figure S13b, Supporting Information). The rate performance analysis of the LFP| $\text{NiNb}_2\text{O}_6$  cell (Figure 8b) shows that by using  $\text{NiNb}_2\text{O}_6$  as anode material, the full cell can cycle up to 20 C with  $58 \text{ mAh g}^{-1}$  capacity and 32.2% capacity retention as compared to 1 C. When comparing the 5 C cycling performance between the LFP| $\text{NiNb}_2\text{O}_6$  cell and an LFP|Li cell (Figure 8c) it can be clearly observed that the cycling stability at such high rates is dramatically enhanced by replacing the lithium metal anode with our  $\text{NiNb}_2\text{O}_6$  anode.

The rate performance and cycling stability of the NCM811| $\text{NiNb}_2\text{O}_6$  cell was also analyzed, and a voltage plateau was observed at the expected 2.05 V (Figure 8d). Cycle life analysis of the NCM811| $\text{NiNb}_2\text{O}_6$  cell after 1000 cycles at 5 C shows a high specific capacity of  $117 \text{ mAh g}^{-1}$  and outstanding cycling stability with a capacity retention of 88.8% and a coulombic efficiency between 99.8 and 100.2% (Figure S13c, Supporting Information). The NCM811| $\text{NiNb}_2\text{O}_6$  cell exhibited a lower capacity retention for higher rates (11% capacity retention at 20 C as compared to 1 C, Figure 8e), than the LFP| $\text{NiNb}_2\text{O}_6$  cell, which can be explained by a lower power density of the NCM811 commercial foil as compared to the LFP foil under high charging current densities. Comparison between the NCM811| $\text{NiNb}_2\text{O}_6$  cell and an NCM811|Li cell (Figure 8f) shows that the cycling stability is also here strongly enhanced by introducing the  $\text{NiNb}_2\text{O}_6$  anode.

Although the full cell studies show that using a  $\text{NiNb}_2\text{O}_6$  electrode combines good cycling ability at high rates with a reasonable operating voltage range, it is still important to determine its electrochemical performance when applying a minimal amount of liquid electrolyte as required in commercial lithium-ion batteries. In order to investigate the electrochemical characteristics of  $\text{NiNb}_2\text{O}_6$  electrodes under lean electrolyte conditions,<sup>[45]</sup> the amount of electrolyte was limited to  $30 \mu\text{L}$  ( $\text{mAh}^{-1}$ ) in strong contrast to the used  $300 \mu\text{L}$  ( $\text{mAh}^{-1}$ ) in the above experiments. The rate performance of  $\text{NiNb}_2\text{O}_6$  in a half cell against lithium metal was still very good, as shown in Figure S14a, Supporting Information, for rates between 1 and 20 C. The voltage versus specific capacity profile during charge-discharge cycling at various rates shows that the average voltage plateau stays constant at around 1.7 V (Figure S14b, Supporting

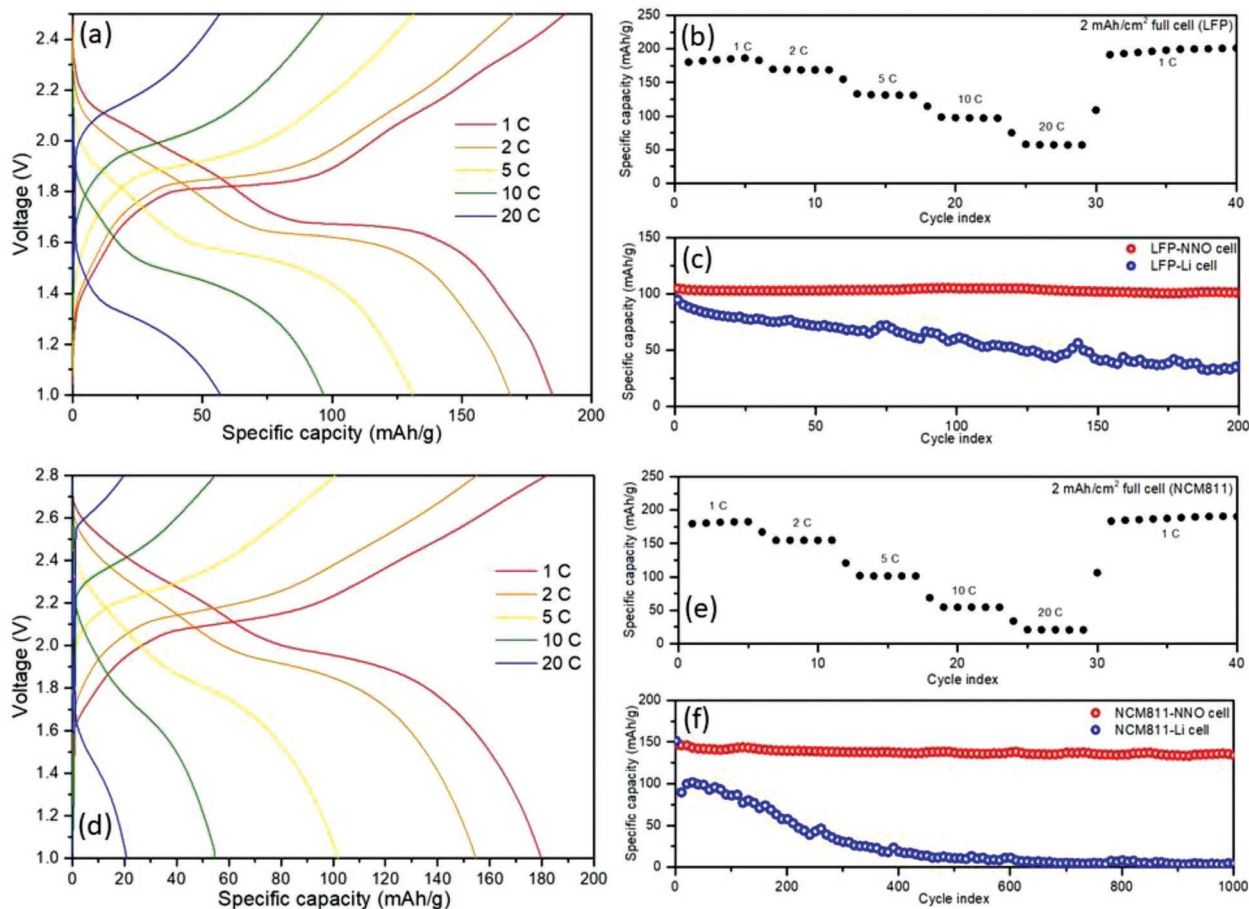


**Figure 8.** a) Voltage versus specific capacity profile of the rate performance test of the  $\text{LiFePO}_4/\text{NiNb}_2\text{O}_6$  cell (using the mass of  $\text{NiNb}_2\text{O}_6$  for specific capacity); b) Specific capacity versus cycle number profile of the rate performance test of the  $\text{LiFePO}_4/\text{NiNb}_2\text{O}_6$  cell (between 1 and 20 C, using the mass of  $\text{NiNb}_2\text{O}_6$  for specific capacity); c) Cycling stability test under 5 C of the  $\text{LiFePO}_4/\text{NiNb}_2\text{O}_6$  and  $\text{LiFePO}_4/\text{Li}$  cell (using the mass of  $\text{LiFePO}_4$  for specific capacity); d) Voltage versus specific capacity profile of the rate performance test of the  $\text{NCM811}/\text{NiNb}_2\text{O}_6$  cell (using the mass of  $\text{NiNb}_2\text{O}_6$  for specific capacity); e) Specific capacity versus cycle number profile of the rate performance test of the  $\text{NCM811}/\text{NiNb}_2\text{O}_6$  cell (between 1 and 20 C, using the mass of  $\text{NiNb}_2\text{O}_6$  for specific capacity); f) Cycling stability test under 5 C of the  $\text{NCM811}/\text{NiNb}_2\text{O}_6$  and  $\text{NCM811}/\text{Li}$  cell (using the mass of  $\text{NCM811}$  for specific capacity).

Information), while the voltage bias between the charge and discharge plateaus increased faster as compared to half cells with a larger amount of liquid electrolyte (Figure 5e). This indicates a faster increase in internal resistance when a minimal amount of electrolyte is used. However, when cycling at 5 C the coulombic efficiency was stable at 100.1% and the reversible capacity was still  $115 \text{ mAh g}^{-1}$  after 600 cycles (Figure S14c, Supporting Information), demonstrating that  $\text{NiNb}_2\text{O}_6$  electrodes also exhibit good cycling ability under lean electrolyte conditions.

### 3. Conclusions

In this work, nickel niobate  $\text{NiNb}_2\text{O}_6$  has been demonstrated for the first time as a new high-rate anode material for lithium-ion batteries. The  $\text{NiNb}_2\text{O}_6$  host crystal structure exhibits only a single type of channel for lithium-ion intercalation leading

to a single voltage plateau at 1.6–1.7 V during charge-discharge cycling. The oxidation of all three transition metal ions (Ni, Nb) enables the structure to fully lithiate up to  $\text{Li}_3\text{NiNb}_2\text{O}_6$  with a capacity of about  $244 \text{ mAh g}^{-1}$  at low current densities. Nickel niobate exhibits a high diffusion coefficient of  $10^{-12} \text{ cm}^2 \text{ s}^{-1}$ , which enables fast (dis)charging at high current densities resulting in high capacities of 220, 165, 140, and  $50 \text{ mAh g}^{-1}$  for respectively 1, 5, 10, and 100C. Furthermore, the minimal volume change during lithiation is the origin of the stable reversible lithiation process in  $\text{NiNb}_2\text{O}_6$  and leads to a capacity retention of 81% after 20 000 cycles at 100C. Finally, full cell systems against  $\text{LiFePO}_4$  and NCM811 cathodes demonstrate the promising energy storage performance of nickel niobate anodes in practical battery devices. Our results strongly suggest that  $\text{NiNb}_2\text{O}_6$  is an intrinsic high-rate anode material without the requirement of realizing nano-architectures as typical for numerous titanium- and niobium-based oxides through complex synthesis procedures to minimize the length scales for lithium diffusion.

## 4. Experimental Section

**Material Synthesis:** The NiNb<sub>2</sub>O<sub>6</sub> powder was synthesized by a simple calcination process following a phase diagram study of this material system in 2005.<sup>[46]</sup> Niobium dioxide (99%, Alfa Aesar) and nickel oxide (99%, Sigma-Aldrich) powders in a molar ratio 1:1 were mixed for 24 h, and subsequently calcined at 1423K for 2 h.

**Material Characterization:** The crystal structure of the synthesized NiNb<sub>2</sub>O<sub>6</sub> powder was studied using X-ray diffraction (PANalytical X'Pert PRO diffractometer with Cu K $\alpha$  radiation and 1/8 slit, in steps of 0.0016° and 10.2 s per step). The morphology and particle size were determined on pristine samples prepared on aluminum foil using SEM (Zeiss Merlin HRSEM). The atomic ratio of nickel and niobium in pristine NiNb<sub>2</sub>O<sub>6</sub> powder was measured by X-ray fluorescence spectroscopy (XRF, Bruker S8 Tiger WDXRF with a Rhodium X-ray Tube), while the oxidation states of nickel and niobium were analyzed by X-ray Photoelectron Spectroscopy (XPS, Omicron Nanotechnology GmbH surface analysis system with a photon energy of 1486.7 eV, Al K $\alpha$  X-ray source). The specific surface area was determined using the Brunauer–Emmett–Teller (BET, Gemini VII of Micromeritics) method. The crystal lattice and grain boundary formation of the NiNb<sub>2</sub>O<sub>6</sub> crystals were determined by Scanning Transmission Electron Microscopy (STEM, Titan Themis TEM with CEOS probe and image aberration corrector operated at 200 KeV).

**Theoretical Modeling:** Spin-polarized DFT calculations were performed using the projector augmented wave (PAW)<sup>[47]</sup> potential method implemented in the Vienna Ab Initio Simulation Package (VASP) code.<sup>[48]</sup> Generalized gradient approximation (GGA) within the scheme of Perdew–Burke–Ernzerhof (PBE)<sup>[49]</sup> was considered as the exchange-correlation XC functional to obtain the atomic structure and diffusion pathway. Total Coulomb energies  $E_c$ , which were carried out to find the most probable favorable sites for Li, were computed with the so-called “supercell” code<sup>[50]</sup> using a  $1 \times 1 \times 2$  (Li<sub>1</sub>Ni<sub>8</sub>Nb<sub>16</sub>O<sub>48</sub>) supercell. To study Li diffusion, ab initio molecular dynamics (AIMD) simulation runs of 65ps were first performed at  $T = 600, 1000, \text{ and } 1200 \text{ K}$  with a time step of 1fs using DFT-PBE. The number of Li jumps between Li sites was not sufficient to compute the diffusion barrier, but the Li pathway was determined to be along the  $c$  direction. The diffusion barrier was then computed using the Nudged Elastic Band (NEB) method with 7 images. For the DFT-NEB and AIMD calculations, a  $1 \times 1 \times 2$  supercell was also used. A  $k$ -point mesh of  $1 \times 1 \times 1$  was applied for these calculations. For the DFT calculations that were carried out to find the minimum total energy structure, a  $k$ -point mesh of  $1 \times 4 \times 2$  was used. For all the calculations, an energy cutoff of 500 eV was used. Electronic and force convergence criteria of  $10^{-4} \text{ eV}$  and  $10^{-3} \text{ eV } \text{\AA}^{-1}$ , respectively, were considered for DFT and NEB calculations. The VESTA program<sup>[51]</sup> was applied to visualize the atomic structures.

**Electrochemical Analysis:** The electrodes were fabricated by mixing the active NiNb<sub>2</sub>O<sub>6</sub> powder, conductive carbon, and binder material with mass ratios of 8:1:1 as well as 7.5:1.5:1 (the latter for rate performance only). The mixtures were pasted on copper foil with 1–3 mg cm<sup>-2</sup> loading in an area of 1 cm<sup>2</sup>. The active NiNb<sub>2</sub>O<sub>6</sub> material and conductive carbon (super p) were ground in an agate mortar and pestle by hand for 30 min. The binder material, polyvinylidene difluoride (PVDF, Mw 27 500, Sigma-Aldrich) was dissolved in N-methyl pyrrolidone (NMP, 99+%, Sigma-Aldrich) with a concentration of 0.05 g mL<sup>-1</sup> by stirring for 48 h. The mixture of NiNb<sub>2</sub>O<sub>6</sub> and conductive carbon was dispersed in the PVDF solution in an ultrasonic bath within 20 min.

All electrochemical tests were conducted in EL-cells (ECC-ref). The mixed NiNb<sub>2</sub>O<sub>6</sub> electrodes were studied as cathode against a lithium metal disk (99.9%, Sigma-Aldrich) anode in a half-cell configuration. The used electrolyte was 1.0 M LiPF<sub>6</sub> in 1:1 ratio v/v ethylene carbonate/dimethyl carbonate (EC/DMC; Sigma-Aldrich, battery grade), together with 1 mm thick glass fiber separators (ECC1-01-0012-B/L). The electrochemistry measurements were performed in a galvanostat/potentiostat (VMP-300, BioLogic) with EC-Lab software at room temperature and the reported potentials were compared to Li<sup>+/</sup>Li.

The electrochemical performance was characterized by galvanostatic charge-discharge cycling, CV, and rate measurements.

Cycle life analysis was performed for three different C rates (1, 5, and 10 C) in order to show the cycling ability of NiNb<sub>2</sub>O<sub>6</sub> under different current densities. The rate performance was studied from 0.5 to 100 C. CV was performed for four different sweep rates (0.1, 0.2, 0.5, and 1 mV s<sup>-1</sup>) in order to obtain lithium-ion diffusion coefficients as well as the pseudo-capacity contributions under different sweep rates. The C-rate in this work was defined by one oxidation state change per one transition metal atom. Thus, the theoretical capacity of NiNb<sub>2</sub>O<sub>6</sub> was calculated by:

$$Q_{\text{theoretical}} = \frac{nF}{3.6 m} = \frac{3 \times 96485.3 \text{ C mol}^{-1}}{3.6 \text{ mA}^{-1} \text{h}^{-1} \times 340.5 \text{ g mol}^{-1}} = 236.14 \text{ mAh g}^{-1} \quad (3)$$

Where  $n$  is the number of electrons transferred per mol,  $F$  is Faraday's constant, 3.6 is a conversion factor from C to mAh, and  $m$  is the molar mass of NiNb<sub>2</sub>O<sub>6</sub>.

Furthermore, EIS and the GITT were used to determine the lithium-ion diffusion coefficients and the resistances of the electrode. EIS analysis was performed between 10 mHz to 100 kHz with 10 mV amplitude at both the charge and discharge stages (i.e., open circuit voltages at 1.2 and 2.6 V). GITT analysis was performed under C/12 rate and by applying current pulses with a 10 min rest period (limitation of the rest is  $dE_{\text{we}}/dt < 0.1 \text{ mV h}^{-1}$ ) in between the pulses.

**Practical Electrochemical Performance Analysis:** The electrochemical performance of NiNb<sub>2</sub>O<sub>6</sub> as anode material was also studied in full cells to determine the achieved enhancement as new electrode material in practical lithium-ion batteries. First, the electrochemical performance of NiNb<sub>2</sub>O<sub>6</sub> electrodes under high loading (about 8.5 mg cm<sup>-2</sup>, 2 mAh cm<sup>-2</sup>) was investigated by repetitive charge-discharge cycling at 1C and rate performance analysis between 1 and 50 C. Second, two full cells were fabricated in which two different cathode materials (LiFePO<sub>4</sub> and LiNi<sub>0.8</sub>Mn<sub>0.1</sub>Co<sub>0.1</sub>O<sub>2</sub> commercial foils, 2 mAh cm<sup>-2</sup>, Customcells Itzehoe GmbH) were incorporated. Both full cells were characterized to determine the electrochemical performance of the large loading NiNb<sub>2</sub>O<sub>6</sub> electrodes versus practical cathodes by charge-discharge cycling at 5C and rate performance analysis between 1 and 20 C. Finally, the high rate performance and cycling stability of NiNb<sub>2</sub>O<sub>6</sub> electrodes was investigated under lean electrolyte conditions (30  $\mu\text{L}$  (mAh)<sup>-1</sup>).

## Supporting Information

Supporting Information is available from the Wiley Online Library or from the author.

## Acknowledgements

R.X. and K.Z. contributed equally to this work. R.X. and J.Z. acknowledge the financial support of the China Scholarships Council (CSC) program, respectively No. 201906150132 and No. 201807720013. The STEM work was performed at the Nanostructure Research Center (NRC), which was supported by the Fundamental Research Funds for the Central Universities (WUT: 2019H1012GX), the State Key Laboratory of Advanced Technology for Materials Synthesis and Processing, and the State Key Laboratory of Silicate Materials for Architectures (all of the laboratories are at Wuhan University of Technology).

## Conflict of Interest

The authors declare no conflict of interest.

## Data Availability Statement

Research data are not shared.

## Keywords

fast charging, high-rate anodes, lithium-ion batteries, lithium-ion diffusivity, nickel niobate, NiNb<sub>2</sub>O<sub>6</sub>

Received: September 24, 2021

Revised: October 22, 2021

Published online:

- 
- [1] J. Y. Ma, X. T. Guo, H. G. Xue, K. M. Pan, C. S. Liu, H. Pang, *Chem. Eng.* **2020**, *380*, 122428.
- [2] M. Uddin, P. K. Alaboina, S. Cho, *Mater. Today Energy* **2017**, *5*, 138.
- [3] H. Y. Geng, Y. Peng, L. T. Qu, H. J. Zhang, M. H. Wu, *Adv. Energy Mater.* **2020**, *10*, 1903030.
- [4] Y. Liu, Y. Zhu, Y. Cui, *Nat. Energy* **2019**, *4*, 540.
- [5] X. Wu, K. Song, X. Zhang, N. Hu, L. Li, W. Li, L. Zhang, H. Zhang, *Front. Energy Res.* **2019**, *7*, 1.
- [6] Q. Wang, B. Mao, S. I. Stolarov, J. Sun, *Prog. Energy Combust. Sci.* **2019**, *73*, 95.
- [7] M. F. Oszajca, M. I. Bodnarchuk, M. V. Kovalenko, *Chem. Mater.* **2014**, *26*, 5422.
- [8] H. Wu, G. Chan, J. W. Choi, I. Ryu, Y. Yao, M. T. McDowell, S. W. Lee, A. Jackson, Y. Yang, L. B. Hu, Y. Cui, *Nat. Nanotechnol.* **2012**, *7*, 310.
- [9] J. Kasnatscheew, T. Placke, B. Streipert, S. Rothermel, R. Wagner, P. Meister, I. C. Laskovic, M. Winter, *J. Electrochem. Soc.* **2017**, *164*, A2479.
- [10] K. Nakahara, R. Nakajima, T. Matsushima, H. Majima, *J. Power Sources* **2003**, *117*, 131.
- [11] C. Li, M. Zhao, C. N. Sun, B. Jin, C. C. Yang, Q. Jiang, *J. Power Sources* **2018**, *397*, 162.
- [12] H. Wei, E. F. Rodriguez, A. F. Hollenkamp, A. I. Bhatt, D. Chen, R. A. Caruso, *Adv. Funct. Mater.* **2017**, *27*, 1703270.
- [13] H. Ren, R. Yu, J. Qi, L. Zhang, Q. Jin, D. Wang, *Adv. Mater.* **2019**, *31*, 1805754.
- [14] F. Su, J. Q. Qin, P. Das, F. Zhou, Z. S. Wu, *Energy Environ. Sci.* **2021**, *14*, 2269.
- [15] V. Augustyn, J. Come, M. A. Lowe, J. W. Kim, P.-L. Taberna, S. H. Tolbert, H. D. Abruña, P. Simon, B. Dunn, *Nat. Mater.* **2013**, *12*, 518.
- [16] Y. Yang, H. Zhu, J. F. Xiao, H. B. Geng, Y. F. Zhang, J. B. Zhao, G. Li, X. L. Wang, C. C. Li, Q. Liu, *Adv. Mater.* **2020**, *32*, 1905295.
- [17] K. J. Griffith, K. M. Wiaderek, G. Cibir, L. E. Marbella, C. P. Grey, *Nature* **2018**, *559*, 556.
- [18] L. Yan, J. Shu, C. Li, X. Cheng, H. Zhu, H. Yu, C. Zhang, Y. Zheng, Y. Xie, Z. Guo, *Energy Storage Mater.* **2019**, *16*, 535.
- [19] W. Ye, H. Yu, X. Cheng, H. Zhu, R. Zheng, T. Liu, N. Long, M. Shui, J. Shu, *Electrochim. Acta* **2018**, *292*, 331.
- [20] L. Yan, X. Cheng, H. Yu, H. Zhu, T. Liu, R. Zheng, R. Zhang, M. Shui, J. Shu, *Energy Storage Mater.* **2018**, *14*, 159.
- [21] I. Yaeger, A. H. Morrish, B. M. Wanklyn, *Phys. Rev. B* **1977**, *15*, 1465.
- [22] V. R. Wichman, H. Muller-Buschbaum, *Z. Anorg. Allg. Chem.* **1983**, *503*, 101.
- [23] T. J. S. Munsie, A. Millington, P. A. Dube, H. A. Dabkowska, J. Britten, G. M. Luke, J. E. Greedan, *J. Solid State Chem.* **2016**, *236*, 19.
- [24] D. J. Fa, B. Yu, Y. Q. Miao, *Colloids Surf. A* **2019**, *564*, 31.
- [25] M. V. Cagnoli, A. M. Alvarez, N. G. Gallegos, J. F. Bengoa, C. D. Duarte de Souza, M. Schmal, S. G. Marchetti, *Appl. Catal., A* **2007**, *326*, 113.
- [26] B. K. Guo, X. Q. Yu, X. G. Sun, M. F. Chi, Z. A. Qiao, J. Liu, Y. S. Hu, X. Q. Yang, J. B. Goodenough, S. Dai, *Energy Environ. Sci.* **2014**, *7*, 2220.
- [27] H. Yildirim, J. Greeley, S. K. R. S. Sankaranarayanan, *J. Phys. Chem. C* **2011**, *115*, 15661.
- [28] J. Meng, Q. He, L. Xu, X. Zhang, F. Liu, X. Wang, Q. Li, X. Xu, G. Zhang, C. Niu, Z. Xiao, Z. Liu, Z. Zhu, Y. Zhao, L. Mai, *Adv. Energy Mater.* **2019**, *9*, 1802695.
- [29] J. Billaud, F. Bouville, T. Magrini, C. Villeveille, A. R. Studart, *Nat. Energy* **2016**, *1*, 16097.
- [30] Y. Y. Zhang, O. I. Malyi, Y. X. Tang, J. Q. Wei, Z. Q. Zhu, H. R. Xia, W. L. Li, J. Guo, X. R. Zhou, Z. Chen, C. Persson, X. D. Chen, *Angew. Chem., Int. Ed.* **2017**, *56*, 14847.
- [31] H. T. Sun, L. Mei, J. F. Liang, Z. P. Zhao, C. Lee, H. L. Fei, M. N. Ding, J. Lau, M. F. Li, C. Wang, X. Xu, G. L. Hao, B. Papandrea, I. Shakir, B. Dunn, Y. Huang, X. F. Duan, *Science* **2017**, *356*, 599.
- [32] H. G. Jung, S. T. Myung, C. S. Yoon, S. B. Son, K. H. Oh, K. Amine, B. Scrosati, Y. K. Sun, *Energy Environ. Sci.* **2011**, *4*, 1345.
- [33] X. H. Ma, L. Cheng, L. L. Li, X. Cao, Y. Y. Ye, Y. Y. Wei, Y. D. Wu, M. L. Sha, Z. F. Zi, J. M. Dai, *Electrochim. Acta* **2020**, *332*, 135380.
- [34] K. J. Griffith, A. C. Forse, J. M. Griffin, C. P. Grey, *J. Am. Chem. Soc.* **2016**, *138*, 8888.
- [35] C. F. Lin, L. Hu, C. B. Cheng, K. Sun, X. K. Guo, Q. Shao, J. B. Li, N. Wang, Z. H. Guo, *Electrochim. Acta* **2018**, *260*, 65.
- [36] J. Wang, J. Polleux, J. Lim, B. Dunn, *J. Phys. Chem. C* **2007**, *111*, 14925.
- [37] X. M. Lou, R. J. Li, X. Z. Zhu, L. J. Luo, Y. J. Chen, C. F. Lin, H. L. Li, X. S. Zhao, *ACS Appl. Mater. Interfaces* **2019**, *11*, 6089.
- [38] E. Deiss, *Electrochim. Acta* **2005**, *50*, 2927.
- [39] W. Choi, H. C. Shin, J. M. Kim, J. Y. Choi, W. S. Yoon, *J. Electrochem. Sci. Technol.* **2020**, *11*, 1.
- [40] C. Ho, I. D. Raistrick, R. A. Huggins, *J. Electrochem. Soc.* **1980**, *127*, 343.
- [41] R. J. Li, Y. R. Pu, J. Xu, Q. F. Fu, G. S. Liang, X. Z. Zhu, L. J. Luo, Y. J. Chen, C. F. Lin, *Ceramics* **2019**, *45*, 12211.
- [42] X. D. Liu, H. Wang, S. Y. Zhang, G. Y. Liu, H. Q. Xie, J. M. Ma, *Electrochim. Acta* **2018**, *292*, 759.
- [43] C. F. Lin, S. J. Deng, H. Shen, G. Z. Wang, Y. F. Li, L. Yu, S. W. Lin, J. B. Li, L. Lu, *J. Alloys Compd.* **2015**, *650*, 616.
- [44] N. Y. Yao, H. K. Liu, X. Liang, Y. Sun, X. Y. Feng, C. H. Chen, H. F. Xiang, *J. Alloys Compd.* **2019**, *771*, 755.
- [45] J. Xiao, Q. Y. Li, Y. J. Bi, M. Cai 3, B. Dunn, T. Glossmann, J. Liu, T. Osaka, R. Sugiura, B. B. Wu, J. H. Yang 2, J. G. Zhang, M. S. Whittingham, *Nat. Energy* **2020**, *5*, 561.
- [46] M. Valant, D. Suvorov, *J. Am. Ceram. Soc.* **2005**, *88*, 2540.
- [47] P. E. Blöchl, *Phys. Rev. B* **1994**, *50*, 17953.
- [48] G. Kresse, J. Furthmüller, *Phys. Rev. B* **1996**, *54*, 11169.
- [49] J. P. Perdew, K. Burke, M. Ernzerhof, *Phys. Rev. Lett.* **1996**, *77*, 3865.
- [50] K. Okhotnikov, T. Charpentier, S. Cadars, *J. Cheminf.* **2016**, *8*, 17.
- [51] K. Momma, F. Izumi, *J. Appl. Crystallogr.* **2011**, *44*, 1272.